Design Method for Quasi-Optimal Multiband Branch-Line Couplers

Luca Piazzon,[1] Paul Saad,[2] Paolo Colantonio,[1] Franco Giannini,[1] Kristoffer Andersson,[2] Christian Fager[2]

[1] Department of Electronics Engineering, University of Roma Tor Vergata, 00133 Roma, Italy
[2] Department of Microtechnology and Nanoscience, Chalmers University of Technology, Gothenburg, Sweden

Received 28 September 2012; accepted 25 January 2013

ABSTRACT: In this article, the design approach, the implementation, and experimental results of multiband branch-line couplers operating at arbitrary frequencies are presented. The conventional branch-line coupler structure is adapted to multiband operation by shunting its four ports with multiband reactive networks. The performance of the proposed multiband couplers is theoretically analyzed and optimized through the even-odd mode circuit analysis. Dual-band (2.4–3.5 GHz), triple-band (1.5–2.4–4.2 GHz), and quad-band (1.5–2.4–3.5 GHz) microstrip branch-line couplers have been realized and tested to verify the design method. The good experimental results (input return loss greater than 15 dB and amplitude imbalance lower than 0.7 dB) show excellent agreement with theoretical and simulated ones, thus validating the proposed approach. © 2013 Wiley Periodicals, Inc. Int J RF and Microwave CAE 24:117–129, 2014.

Keywords: balanced; branch-line; coupler; multiband; passive

I. INTRODUCTION

The fast development of wireless communication systems and the roll-out of new standards, such as GSM (800/900/1800 MHz), WCDMA (2.1 GHz), WLAN (2.45/5.25 GHz), and WiMAX (3.5 GHz), requires multiband transceivers [1] to process several types of signals at the same time. Among different combining passive structures, the branch-line coupler is one of the most important components used in microwave and millimeter-wave applications because of its essential role in balanced [2] and Doherty amplifiers [3, 4], mixers [5], modulators [6] and beam forming networks for circularly polarized antennas [7] due to its good directivity, and inherent 90° phase shift between its output ports. As a consequence, a method for the design of multiband branch-line couplers can be of key importance for the development of multiband transceivers.

Recently, different configurations for the design of dual-band branch-line couplers have been proposed [8–21]. One of the most adopted solutions is based on the replacement of the quarter-wave transmission lines of the branch-line coupler with an equivalent dual-band network [8–13]. Alternative approaches are proposed in [14] and [15], where the coupling between microstrip lines is successfully exploited, in [16], where the three-branch-line topology is proposed, in [17], where the concept of stub-loaded rectangular patch is introduced, and in [18], where the dual-band operation is obtained by adding a properly designed series transmission line section at the four ports of the single-band branch-line coupler. The capability of implementing dual-band branch-line couplers by means of composite right/left-handed transmission lines has also been demonstrated in [19–21]. However, all the mentioned configurations were developed only for dual-band operations.

Solutions to design branch-line couplers having more than two operating bands can be found in [22–26]. However, the methods proposed in [22–24] are not assisted with a full theoretical analysis that demonstrates the possibility to extend them for an arbitrary number of operating frequencies. Moreover, the approach presented in [25] is limited to correlated frequencies, while the one adopted in [26] exploits the composite right/left handed transmission line concept, resulting in degraded performance and high losses due to the complexity of the circuit and the critical

Correspondence to: L. Piazzon; e-mail: luca.piazzon@uniroma2.it)
DOI 10.1002/mmce.20723
Published online 8 April 2013 in Wiley Online Library (wileyonlinelibrary.com).

dimensions of some of its constitutive semilumped elements.

In this article, drastically extending [27], a closed form design approach for multiband branch-line couplers for arbitrary operating frequencies is presented. Starting from the dual-band quarter-wave transmission line topology, an optimization technique is proposed to extend its behavior to three arbitrary bands. Later, the method is generalized for any number of arbitrary bands. The design approach is thereafter demonstrated through the practical implementation of dual-band, triple-band, and quad-band microstrip branch-line couplers. The experimental measurements validate the proposed design methodology, showing excellent results in terms of matching, directivity, phase quadrature and isolation at each operating frequency band.

II. THEORETICAL ANALYSIS AND DESIGN EQUATIONS

The conventional (single-band) branch-line coupler is composed of four quarter-wave transmission lines [28]. Hence, the design of the multiband branch-line coupler starts from the investigation of a suitable topology to achieve multiband quarter-wave transmission lines. Then, by combining four of such structures, the multiband branch-line coupler is achieved.

A. Dual-Band Quarter-Wave Transmission Line

The ABCD-matrix of a quarter-wave transmission line having characteristic impedance Z_T is given by[28]

$$ABCD_{\lambda/4} = \begin{bmatrix} 0 & jZ_T \\ \frac{j}{Z_T} & 0 \end{bmatrix} \tag{1}$$

The matrix in (1) can be simultaneously produced at two arbitrary frequencies (f_i with $i = 1,2$) by means of the network in Figure 1 [9]. It consists of a series transmission line, having characteristic impedance Z_c, and two purely reactive shunting elements (B_i). The ABCD-matrix of the topology in Figure 1 at the two frequencies is given by:

$$ABCD_{f_i} = \begin{bmatrix} 1 & 0 \\ jB_i & 1 \end{bmatrix} \begin{bmatrix} \cos\theta_i & jZ_c \sin\theta_i \\ \frac{j}{Z_c}\sin\theta_i & \cos\theta_i \end{bmatrix} \begin{bmatrix} 1 & 0 \\ jB_i & 1 \end{bmatrix} \tag{2}$$

where $\theta_i = \frac{\pi f_i}{2 f_c}$. In Ref. 9, it has been demonstrated that by equating (2) to (1) leads to the following constraints for the topology in Figure 1:

$$f_c = \frac{f_1 + f_2}{2} \tag{3}$$

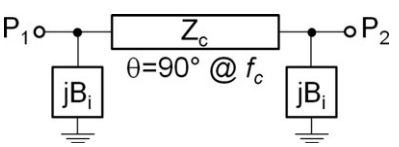

Figure 1 Π-shaped network which is equivalent to a quarter-wave transmission line at two frequencies. B_i, $i = 1,2$, represent the susceptances at the two frequencies.

$$Z_{c,i} = \frac{Z_T}{\sin\left(\frac{\pi}{2}\cdot\frac{f_i}{f_c}\right)} \tag{4}$$

$$B_i = \frac{1}{Z_c \tan\left(\frac{\pi}{2}\cdot\frac{f_i}{f_c}\right)} \tag{5}$$

Being $Z_{c,1} = Z_{c,2}$ in (4), the design parameter Z_c of the network in Figure 1 is unique, allowing the ABCD-matrix in (1) to be obtained at both frequencies without any compromise. It has to remark that (4) has valid solutions, that is, positive values for $Z_{c,i}$, only if $0 < f_i/f_c < 2$. Accounting for (3), this condition is verified if both frequencies are greater than 0.

B. Triple-Band Quarter-Wave Transmission Line

Assuming three arbitrary frequencies ($0 < f_1 < f_2 < f_3$), a unique Z_c solution is not derivable from (4), since the sine function allows a unique solution only for two angles symmetrically positioned with respect to 90°. Therefore, it is not possible to exactly reproduce the ABCD-matrix in (1) at the three frequencies, simultaneously. However, by properly choosing the design parameters of the network in Figure 1, it is possible to find a condition in which the resulting matrix at the three frequencies is as close as possible to (1).

To infer the optimum design parameters, it is useful to start performing the matrix products in (2). Moreover, the relation in (5) has to be adopted to define the proper B_i values to guarantee that the network in Figure 1 behaves as a quarter-wave transmission line at all operating frequencies. The resulting ABCD-matrix is

$$ABCD_{f_i} = \begin{bmatrix} 0 & jZ_c \sin\left(\frac{\pi f_i}{2 f_c}\right) \\ \frac{j}{Z_c \sin\left(\frac{\pi f_i}{2 f_c}\right)} & 0 \end{bmatrix} \tag{6}$$

From the ABCD-matrix in (6) the full two-ports scattering-parameters matrix can be derived. However, to reduce the scattering parameters to consider for the analysis, it is useful to account for the properties of the network in Figure 1. In particular, due to the symmetry of the network, $S_{11} = S_{22}$. Moreover, assuming passive and lossless elements, it follows that $S_{21} = S_{12}$ and $|S_{21}|^2 = 1 - |S_{11}|^2$ [28-Section IV.C]. Finally, one can consider that the condition $\angle S_{21} = -90°$ is guaranteed by using (5) to calculate the values of B_i [9]. The derived conditions are valid at each frequency, independent of the value selected for f_c and Z_c. As a consequence, only the S_{11} parameter can be considered in the analysis. It is given by:

$$S_{11} = \frac{B - CZ_0^2}{B + CZ_0^2} \tag{7}$$

where Z_0 is the reference impedance of input and output ports. Substituting (6) in (7) leads to

$$S_{11,f_i} = \frac{Z_c^2 \sin^2\left(\frac{\pi f_i}{2 f_c}\right) - Z_0^2}{Z_c^2 \sin^2\left(\frac{\pi f_i}{2 f_c}\right) + Z_0^2} \tag{8}$$

The aim is to find the values of Z_c and f_c, if they exist, that allow to obtain from the network in Figure 1 the same behavior at the three operating frequencies. This task is thus represented by the following condition:

$$|S_{11,f_1}| = |S_{11,f_2}| = |S_{11,f_3}| \tag{9}$$

By substituting (8) in (9), the following sets of possible solutions are derived:

$$\sin\left(\frac{\pi f_1}{2 f_c}\right) = \sin\left(\frac{\pi f_2}{2 f_c}\right) \quad Z_c = \frac{Z_0}{\sqrt{\sin\left(\frac{\pi f_1}{2 f_c}\right)\sin\left(\frac{\pi f_3}{2 f_c}\right)}} \tag{10a}$$

$$\sin\left(\frac{\pi f_1}{2 f_c}\right) = \sin\left(\frac{\pi f_3}{2 f_c}\right) \quad Z_c = \frac{Z_0}{\sqrt{\sin\left(\frac{\pi f_1}{2 f_c}\right)\sin\left(\frac{\pi f_2}{2 f_c}\right)}} \tag{10b}$$

$$\sin\left(\frac{\pi f_2}{2 f_c}\right) = \sin\left(\frac{\pi f_3}{2 f_c}\right) \quad Z_c = \frac{Z_0}{\sqrt{\sin\left(\frac{\pi f_1}{2 f_c}\right)\sin\left(\frac{\pi f_2}{2 f_c}\right)}} \tag{10c}$$

By assuming $Z_0 = Z_T$ and by manipulating (4), the following relations are obtained:

$$\sin\left(\frac{\pi f_1}{2 f_c}\right) = \frac{Z_0}{Z_{c,1}} \tag{11a}$$

$$\sin\left(\frac{\pi f_2}{2 f_c}\right) = \frac{Z_0}{Z_{c,2}} \tag{11b}$$

$$\sin\left(\frac{\pi f_3}{2 f_c}\right) = \frac{Z_0}{Z_{c,3}} \tag{11c}$$

Finally, by replacing (11) in the right side equations of (10), the possible sets of solutions for f_c and Z_c that verify condition (9) are given by

$$f_c = \frac{f_1 + f_2}{2} \quad Z_c = \sqrt{Z_{c,3} \cdot Z_{c,2}} \tag{12a}$$

$$f_c = \frac{f_1 + f_3}{2} \quad Z_c = \sqrt{Z_{c,2} \cdot Z_{c,1}} \tag{12b}$$

$$f_c = \frac{f_2 + f_3}{2} \quad Z_c = \sqrt{Z_{c,1} \cdot Z_{c,2}} \tag{12c}$$

where (12a), (12b), and (12c) are derived by accounting for (10a), (10b), and (10c), respectively. Among the three possible solutions in (12), the optimum one is represented by the solution that minimizes the $|S_{11}|$. By substituting (10) and (12) in (8) and selecting $i = 1$, the following relations are derived for the S_{11} in the three cases:

$$S_{11} = \frac{\sin\left(\pi\frac{f_1}{f_1+f_2}\right) - \sin\left(\pi\frac{f_3}{f_1+f_2}\right)}{\sin\left(\pi\frac{f_1}{f_1+f_2}\right) + \sin\left(\pi\frac{f_3}{f_1+f_2}\right)} \tag{13a}$$

$$S_{11} = \frac{\sin\left(\pi\frac{f_1}{f_1+f_3}\right) - \sin\left(\pi\frac{f_2}{f_1+f_3}\right)}{\sin\left(\pi\frac{f_1}{f_1+f_3}\right) + \sin\left(\pi\frac{f_2}{f_1+f_3}\right)} \tag{13b}$$

$$S_{11} = \frac{\sin\left(\pi\frac{f_1}{f_2+f_3}\right) - \sin\left(\pi\frac{f_2}{f_2+f_3}\right)}{\sin\left(\pi\frac{f_1}{f_2+f_3}\right) + \sin\left(\pi\frac{f_2}{f_2+f_3}\right)} \tag{13c}$$

In Appendix 6 it is demonstrated that the $|S_{11}|$ obtained from (13b) is the minimum respect to (13a) and (13c), independently by the selected operating frequencies. As a consequence, the optimum choice for f_c and Z_c is represented by (12b).

A graphical example that clarifies the inferred solution is reported in Figure 2. For this example $f_1 = 0.6$ GHz, $f_2 = 0.9$ GHz, and $f_3 = 1.4$ GHz are assumed. The solid line in all graphs of Figure 2 depicts the function (4) normalized to Z_T and plotted versus the normalized frequency (f/f_c). Moreover, the discrete frequency variable f_i in (4) has been replaced with the continuous one f to present the continuous behavior of the function. The symbols in the graphs of Figure 2 are $Z_{c,1}$, $Z_{c,2}$ and $Z_{c,3}$ derived by (4). Furthermore, equations (12a), (12b), and (12c) have been used to define f_c in Figures 2a–2c, respectively. It is possible to note that the case reported in Figure 2b is the one that minimizes the distance between the largest ($Z_{c,max}$ in Figure 2) and smallest ($Z_{c,min}$ in Figure 2) values of the three $Z_{c,i}$. As a consequence, the value derived from (12b) for Z_c is as close as possible to all the ideal $Z_{c,i}$, allowing to obtain a better $|S_{11}|$ parameter for the network in Figure 1.

Once we derived the optimum value for f_c and Z_c, the shunted elements at each frequency (B_i) can be easily calculated by using (5). To synthesize the computed B_i, many approaches could be addressed, based on both distributed and/or lumped elements[23, 26, 29–31]. An optimum solution cannot be generalized since it depends on application constraints like size, losses, repeatability, cost, easiness of realization, robustness, model availability and so on. Obviously, considering mass production, the repeatability is in general much more important than losses, while it could be the opposite for a single specialized design. As a consequence, one can consider the approach here adopted as one of the possible solutions and not necessarily the unique and/or the best one. In this work we have chosen to implement the Impedance Buffer Methodology, already proposed in Refs. 29 and 32. Such an approach allows arbitrary reactive loads to be synthesized at an unlimited number of arbitrary frequencies. Moreover, it has the advantages of being based on closed form design equations and to being easily implemented by using distributed planar elements. The structure obtained with the Impedance Buffer Methodology is the ladder

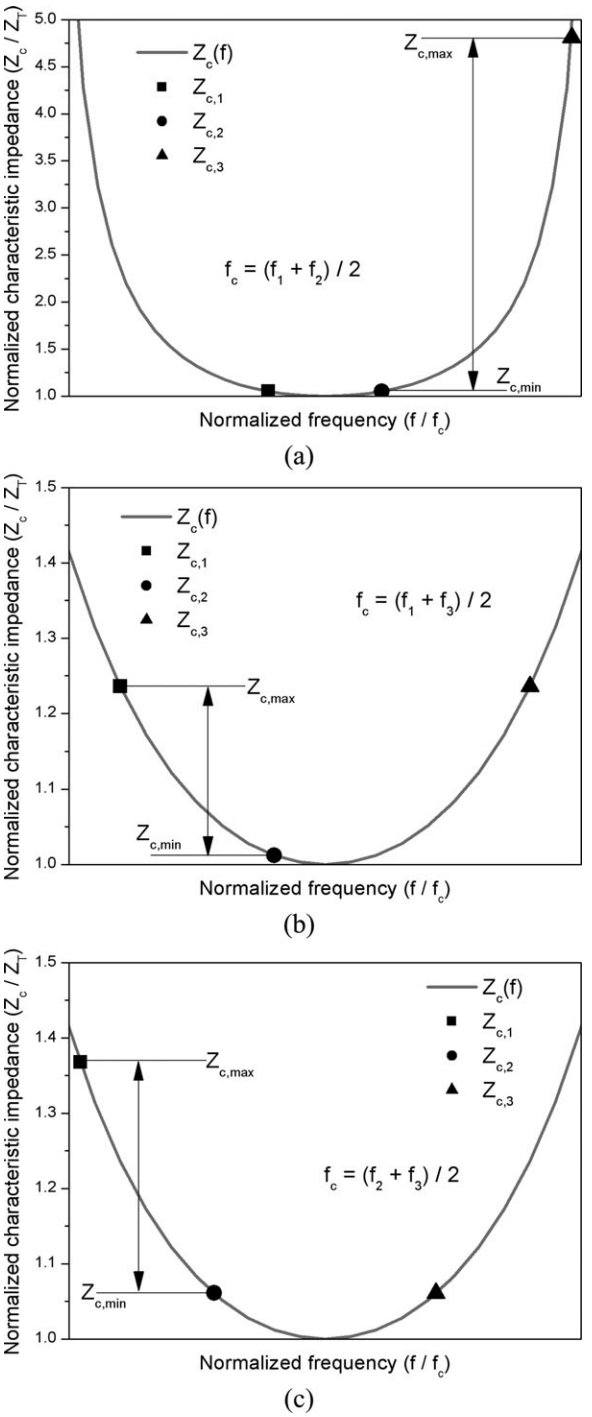

Figure 2 Behavior of Z_c from (4) and values of $Z_{c,i}$ for a triple-band quarter-wave transmission line case by assuming f_c as defined in (a) equation (12a), (b) equation (12b), and (c) equation (12c). For this example $f_1 = 0.6$ GHz, $f_2 = 0.9$ GHz, and $f_3 = 1.4$ GHz are assumed.

network schematically shown in Figure 3. Starting from the input port of the network (P_1 in Figure 3), the operating frequencies are controlled in descending order, that is, from f_3 to f_1. The impedance buffers at f_3 and f_2 are realized by means of a 90° open circuit stub, while the one at f_1 is obtained with a ground connection to reduce the size of the structure. Obviously, depending on the actual application, this may or may not be a desirable feature. The electrical length of each series transmission line (θ_1, θ_2, and θ_3 in Figure 3) can be directly computed from the desired B_i values and the operating frequencies as described in [32].

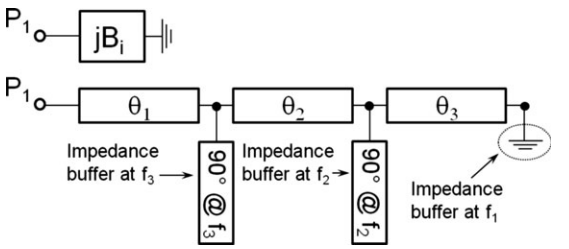

Figure 3 Ladder network obtained applying the Impedance Buffer Methodology to synthesize the B_i susceptances for a triple-band quarter-wave transmission line.

C. Generalization for an arbitrary number of frequencies

The approach presented in the previous subsection can be easily generalized for an arbitrary number (N) of uncorrelated frequencies (i.e., $f_1 < f_2 < \ldots < f_N$). Increasing the number of frequencies, in fact, means increasing the values of $Z_{c,i}$ obtained from (4), as graphically highlighted in Figure 4. In such a graph each symbol indicates examples of hypothetical $Z_{c,i}$ values for each normalized frequency.

Once again an optimum trade-off has to be adopted to select the design parameters, since only one value is usable for the actual implementation of Z_c. However, the higher number of frequencies does not increase the complexity of the problem. Looking at Figure 4, it is possible to note that the general case can be traced to the case of

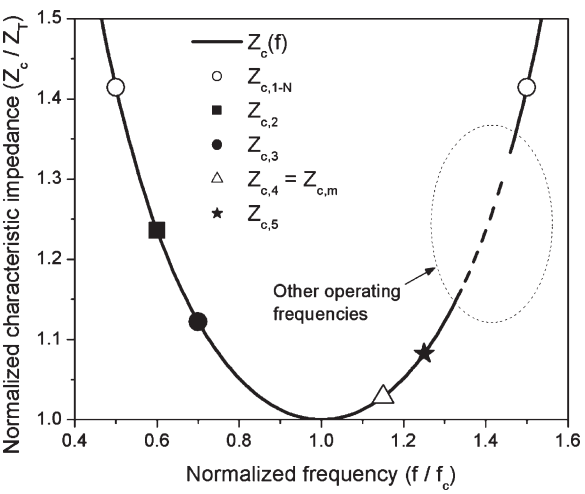

Figure 4 Behavior of Z_c from (4) and values of $Z_{c,i}$ for a multiband quarter-wave transmission line case. For this example $f_1 = 0.5$ GHz, $f_2 = 0.6$ GHz, $f_3 = 0.7$ GHz, $f_4 = 1.15$ GHz, $f_5 = 1.25$ GHz, and $f_N = 1.5$ GHz are assumed. Other arbitrary operating frequencies are supposed in the range 1.35–1.45 GHz as well.

three frequencies. In fact, referring to Figure 4, the design parameters f_c and Z_c can be selected as demonstrated in the previous section, simply considering for the computation the frequencies f_1, f_N, and f_4. Obtaining, thus, $|S_{11,f_1}|=|S_{11,f_4}|=|S_{11,f_N}|$. Moreover, the return loss at the other operating frequencies is better than the one at f_1, f_N and f_4, since the obtained value for Z_c is closest to the ideal $Z_{c,i}$ of these frequencies.

Thus, the generalized design equations for a multiband quarter-wave transmission line derived by applying this approach are the followings:

$$f_c = \frac{f_1 + f_N}{2} \tag{14a}$$

$$Z_{c,i} = \frac{Z_T}{\sin\left(\frac{\pi}{2}\cdot\frac{f_i}{f_c}\right)} \qquad i = 1,2\ldots N \tag{14b}$$

$$Z_{c,m} = \min\left(Z_{c,i}\right) \qquad i = 2,3\ldots N-1 \tag{14c}$$

$$Z_c = \sqrt{Z_{c,1}\cdot Z_{c,m}} \tag{14d}$$

$$B_i = \frac{1}{Z_c\cdot\tan\left(\frac{\pi}{2}\cdot\frac{f_i}{f_c}\right)} \qquad i = 1,2\ldots N \tag{14e}$$

By looking at (14) it is possible to note that this system of equations is practically extended from the dual-band case, where the design is fixed from the boundary frequencies (specifically f_1 and f_N) and the other bands are optimized with a goal of minimum return loss with suboptimal solution.

To synthesize the B_i susceptances for an arbitrary number of operating frequencies, the Impedance Buffer Methodology can be adopted also in this case. This is accomplished by adding an impedance buffer and a series transmission line for each further frequency in Figure 3.

D. D. Limitations of Multiband Quarter-Wave Transmission Lines

This subsection is focused on the analysis of the limitations of the multiband quarter-wave transmission line synthesis presented in the previous subsections. The synthesis method is oriented to identify the best trade-off that equalizes the scattering parameters, and in particular the $|S_{11}|$ parameter, across all the operating frequencies. However, the absolute $|S_{11}|$ value depends on the relation between the operating frequencies. For example, Figure 5 reports two hypothetical cases of $Z_{c,i}$. For sake of clarity, only the boundary values are reported, that is, $Z_{c,1}$, $Z_{c,N}$ and $Z_{c,m}$. In both cases the same f_1 and f_N are assumed, resulting in the same f_c, while the value of f_m is different, resulting in a different value for the actual Z_c from (14d). In particular, the spread between $Z_{c,1\&N}$ and $Z_{c,m}$ in Case-I is smaller than the one of Case-II. Consequently, the $|S_{11}|$ achievable in Case-I is better than the one resulted in Case-II, even if the optimum trade-off is adopted for both.

From the designer point of view it is useful to establish the matching limitation of the structure directly from the operating frequencies. Considering that the worst

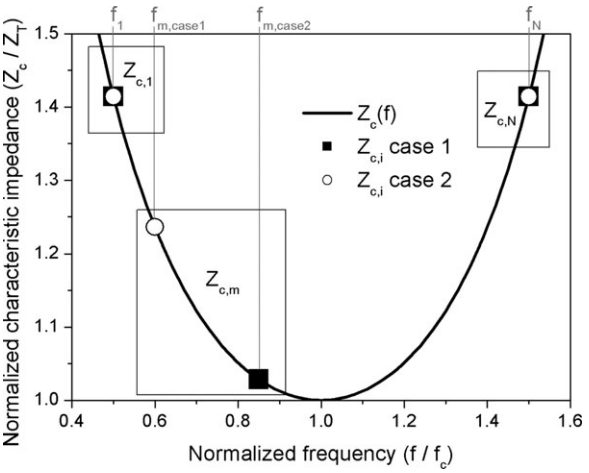

Figure 5 Behavior of Z_c from (4) and two cases of $Z_{c,i}$ having different matching limitations. For both cases $f_1 = 0.5$ GHz and $f_N = 1.5$ GHz are assumed, resulting in the same f_c, $Z_{c,1}$, and $Z_{c,N}$ values. $f_m = 0.6$ GHz and $f_m = 0.85$ GHz are assumed for Case-I and Case-II, respectively.

matching condition occurs simultaneously at f_1, f_m and f_N, it is possible to estimate the achievable matching simply computing the $|S_{11}|$ at f_1 from (13):

$$\left|S_{11,f_1}\right| = \left|\frac{\sin\left(\pi\cdot\frac{f_1}{f_1+f_N}\right) - \sin\left(\pi\cdot\frac{f_m}{f_1+f_N}\right)}{\sin\left(\pi\cdot\frac{f_1}{f_1+f_N}\right) + \sin\left(\pi\cdot\frac{f_m}{f_1+f_N}\right)}\right| \tag{15}$$

To have an idea of the matching limitations, Figure 6 reports the behavior of (15). For illustrative purposes, the frequency axis has been normalized with the function

$$f_{\text{norm}} = \frac{2f - (f_1 + f_N)}{f_N - f_1} \tag{16}$$

Consequently, the values $f_{\text{norm}} = -1$ and $f_{\text{norm}} = 1$ represent the frequencies f_1 and f_N, respectively, independent of their

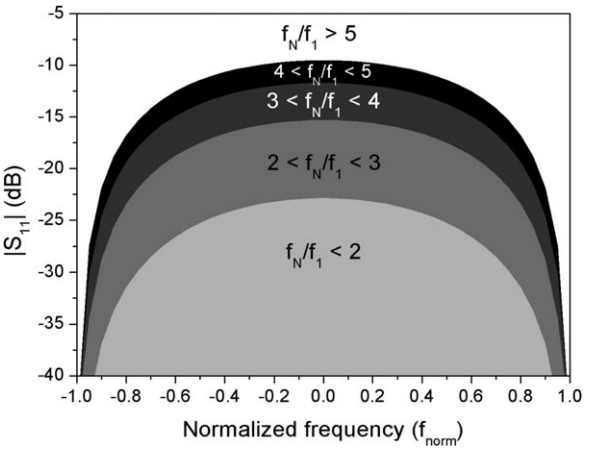

Figure 6 Matching limitation for multiband quarter-wave transmission lines versus normalized frequency f_{norm} as defined in (16).

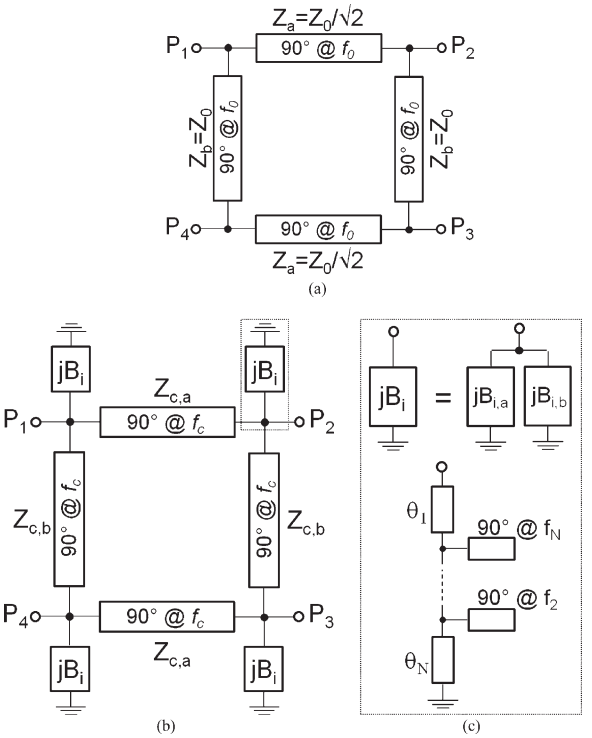

Figure 7 Topology of (a) single-band branch-line coupler, (b) multiband branch-line coupler, and (c) multi-band network for the synthesis of the B_i susceptances.

ratio and absolute value. Moreover, f_m can assume any value between -1 and 1, resulting in $f_{\text{norm}} = 0$ for the case $f_m = f_c$.

Referring to Figure 6, the achievable matching degrades when the ratio between f_N and f_1 increases. At the same time, it depends on the relative position of f_m, resulting in to the worst condition for the case $f_m = f_c$, where also the spread between $Z_{c,1\&N}$ and $Z_{c,m}$ is largest.

E. From the Multiband Quarter-Wave Transmission Line to the Multiband Branch-Line Coupler

The single-band branch-line coupler is obtained by properly combining four single-band quarter-wave transmission lines, as reported in Figure 7a. To achieve the multiband branch-line coupler topology, each single-band quarter-wave transmission line has to be replaced with the multiband equivalent one, following the design methodology described above. Such a procedure leads to a structure similar to the one depicted in Figure 7b. In particular, the values $Z_{c,a}$ and $Z_{c,b}$ are derived substituting $Z_T = Z_a$ and $Z_T = Z_b$ in (14b), respectively, where $Z_a = Z_0\sqrt{2}$ and $Z_b = Z_0$ are the characteristic impedances adopted in the single-band branch line coupler, as shown in Figure 7a [28]. Such operation allows the values of $B_{i,a}$ and $B_{i,b}$ to be calculated as well. Their shunt connection, that is, algebraic sum, leads to the susceptances B_i in Figure 7b. Finally, adopting the Impedance Buffer Methodology, a multiband network having the form depicted in Figure 7c is derived to synthesize the proper B_i susceptance at each operating frequency.

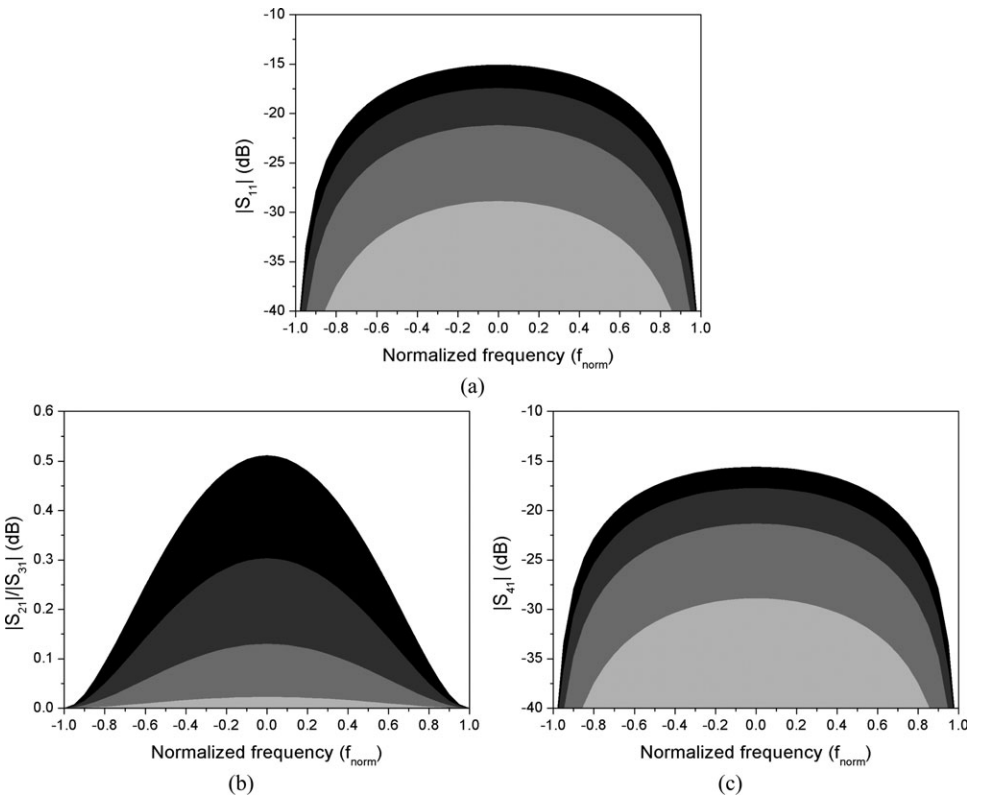

Figure 8 Matching (a), balancing (b) and isolation (c) limitations for multiband branch-line couplers versus normalized frequency f_{norm} as defined in (16).

TABLE I Design Parameters of the Dual-, Triple-, and Quad-Band Branch-Line Couplers

	$Z_a = 50/\sqrt{2}\ \Omega$	$Z_b = 50\ \Omega$
Dual-band branch-line coupler		
$Z_{c,1} = Z_{c,2} = Z_c\ (\Omega)$	36.9	52.2
$B_1 = -B_2$ (mS)	8.2	5.8
Triple-band branch-line coupler		
$Z_{c,1} = Z_{c,3}\ (\Omega)$	48.1	68.0
$Z_{c,2}\ (\Omega)$	36.5	51.6
$Z_c\ (\Omega)$	41.9	59.2
$B_1 = -B_3$ (mS)	22.0	16.0
B_2 (mS)	6.0	4.3
Quad-band branch-line coupler		
$Z_{c,3}\ (\Omega)$	37.8	53.4
B_3 (mS)	−9.0	−6.3

F. Limitations of Multiband Branch-Line Couplers

Previously, it has been demonstrated that selecting $Z_c = \sqrt{Z_{c,1} \cdot Z_{c,m}}$ allows the matching error in a multiband quarter-wave transmission line to be equalized. However, the effect that such choice has on the branch-line coupler in terms of matching, balance and isolation conditions should be verified. The analytical demonstration is presented in Appendix 7. The results show that, by applying the same trade-off for the characteristic impedances of the multiband quarter-wave transmission lines also in the branch-line coupler, the error in the mismatch, imbalance and isolation performance is equally distributed between f_1, f_m, and f_N. At the same time, it is demonstrated that the phase relation between the signals at port 2 and 3 is equal to 90° at each operating frequency, allowing the desired quadrature relation to be obtained.

As was previously demonstrated for the multiband quarter-wave transmission line, it is also possible to relate the limitations of the multiband branch-line coupler directly to the operating frequencies. Referring to Appendix 7, the matching ($|S_{11}|$), balancing ($|S_{21}|/|S_{31}|$) and isolation ($|S_{41}|$) limitations are given by

$$|S_{11}| = \left|\frac{\sin^2\theta_1 - \sin^2\theta_m}{\sin^2\theta_1 + 6\sin\theta_1\sin\theta_m + \sin^2\theta_m}\right| \tag{17a}$$

$$\frac{|S_{21}|}{|S_{31}|} = \left|\frac{\sin\theta_1 + \sin\theta_m}{2\sqrt{\sin\theta_1\sin\theta_m}}\right| \tag{17b}$$

$$|S_{41}| = 2\left|\frac{\sqrt{\sin\theta_1\sin\theta_m}(\sin\theta_1 - \sin\theta_m)}{\sin^2\theta_1 + 6\sin\theta_1\sin\theta_m + \sin^2\theta_m}\right| \tag{17c}$$

where $\theta_1 = \pi\frac{f_1}{f_1+f_N}$ and $\theta_m = \pi\frac{f_m}{f_1+f_N}$. Figure 8 reports the behaviors of (17) as function of f_m and the ratio f_N/f_1, applying the frequency normalization defined in (16).

The behaviors in Figure 8 highlight that the worst condition for the multiband branch-line coupler limitations occur for the case $f_m = f_c$, as was also obtained for the multiband quarter-wave transmission line. However, comparing Figures 8a and 6, it is evident that the branch-line coupler permits a better matching performance compared to the multiband quarter-wave transmission line for the same f_m and f_N/f_1 condition. Moreover, the imbalance performance, reported in Figure 8b, increases for higher ratio f_N/f_1. However, the balance performance is maintained lower than 0.5dB up to $f_N/f_1 = 5$. Finally, referring to Figure 8c, it is possible to note that the behavior of the isolation between ports 1 and 4 is similar to the one of the matching.

III. IMPLEMENTATION OF TEST CIRCUITS

Dual-, triple-, and quad-band branch-line couplers were implemented to demonstrate the validity of the multiband branch-line coupler synthesis approach. All the designed branch-line couplers were implemented on a Rogers 5870 substrate with $\varepsilon_r = 2.33$ and thickness of 0.787 mm.

A. Dual-Band Branch-Line Coupler

For the dual-band branch-line coupler, the selected operating frequencies are $f_1 = 2.4$ GHz and $f_2 = 3.5$ GHz, resulting in $f_c = 2.95$ GHz. The theoretical design parameters are summarized in Table I. In particular, the column $Z_a = 50/\sqrt{2}\ \Omega$ reports the design parameters derived by

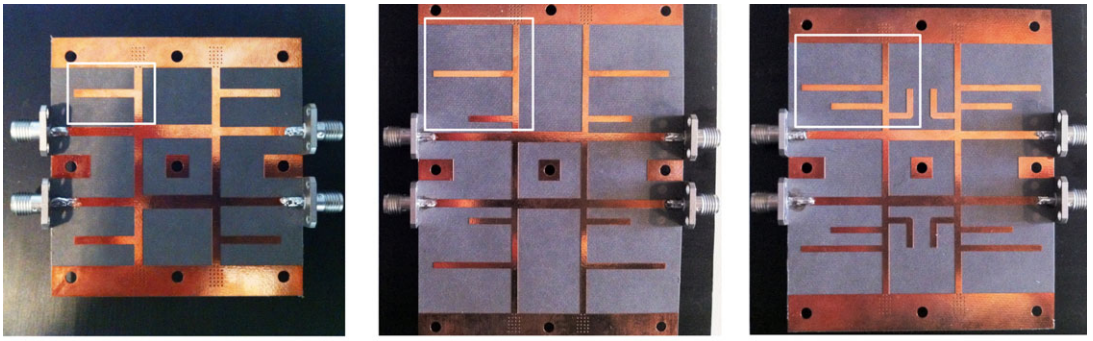

Figure 9 Photos of the realized (a) dual-band, (b) triple-band, and (c) quad-band branch line couplers, whose sizes are 65 × 51 mm^2, 75 × 82 mm^2 and 73 × 70 mm^2, respectively. The network based on the Impedance Buffer Methodology that synthesizes the desired values of B_i is highlighted in each figure by means of a white frame.

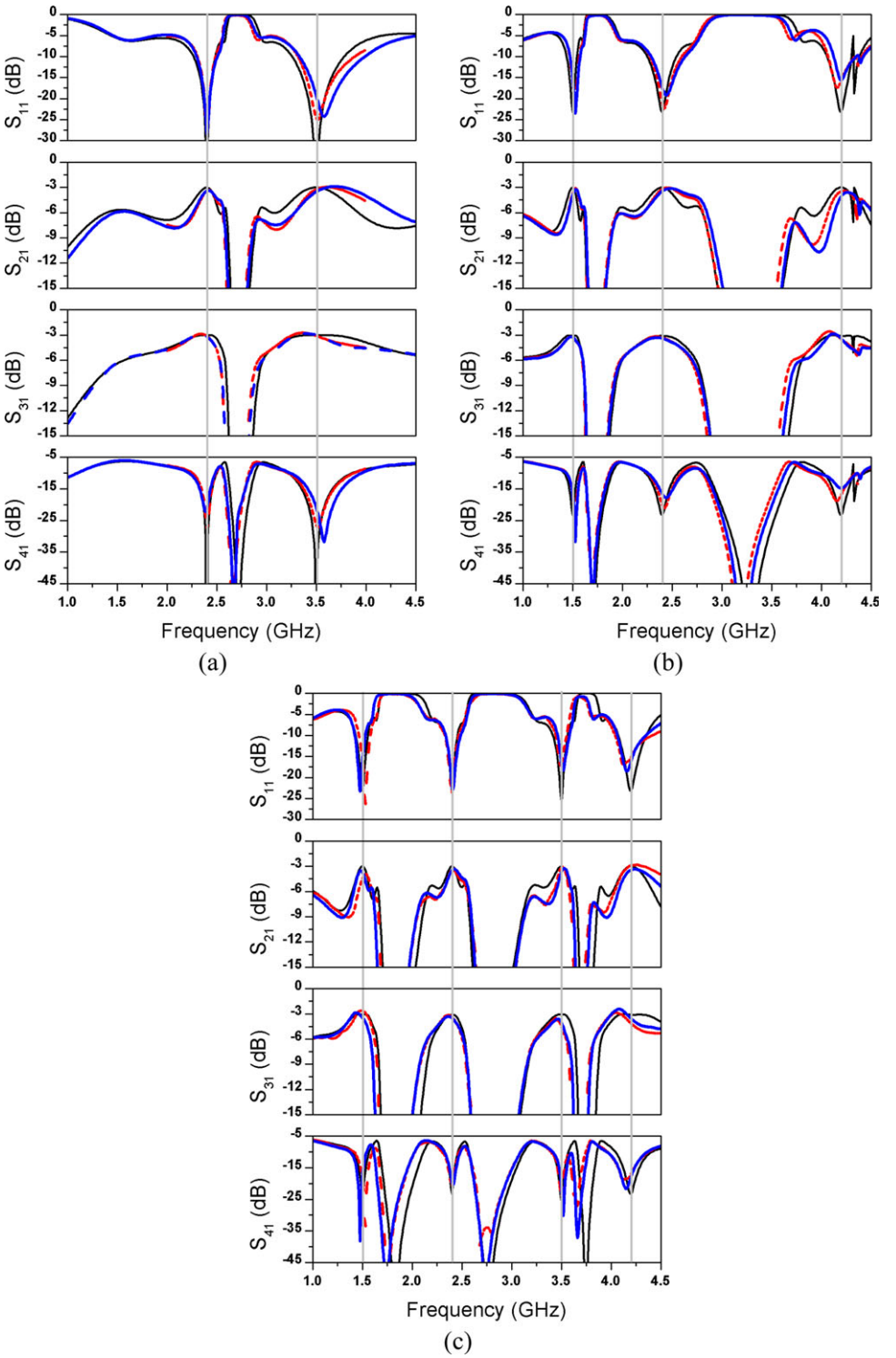

Figure 10 Measured and simulated results of the (a) dual-band, (b) triple-band, and (c) quad-band branch line couplers.

assuming $Z_T = Z_a$ in (14b), while the column $Z_b = 50\ \Omega$ reports the design parameters derived by assuming $Z_T = Z_b$ in (14b). The photo of the realized dual-band branch-line coupler is shown in Figure 9a.

B. Triple-Band Branch-Line Coupler

For the triple-band branch-line coupler, the arbitrarily selected operating frequencies are $f_1 = 1.5$ GHz, $f_2 = 2.4$

TABLE II Measured Results

Parameter	1.5 GHz	2.4 GHz	3.5 GHz	4.2 GHz
Dual-band branch-line coupler				
$\|S_{11}\|$ (dB)	–	−28.36	−19.44	–
$\|S_{21}\|$ (dB)	–	−3.41	−3.50	–
$\|S_{31}\|$ (dB)	–	−3.20	−3.01	–
$\|S_{41}\|$ (dB)	–	−21.29	−21.07	–
ΔA (dB)	–	0.21	0.49	–
$\Delta\phi$ (°)	–	90.49	89.78	–
BW at $\Delta A = 1$ dB (MHz)	–	80	220	–
BW at $\Delta\phi = 90 \pm 5$ (MHz)	–	130	>1000	–
Triple-band branch-line coupler				
$\|S_{11}\|$ (dB)	−15.54	−17.29	–	−15.66
$\|S_{21}\|$ (dB)	−3.85	−3.46	–	−4.08
$\|S_{31}\|$ (dB)	−3.27	−3.39	–	−3.39
$\|S_{41}\|$ (dB)	−17.12	−16.53	–	−14.79
ΔA (dB)	0.58	0.07	–	0.69
$\Delta\phi$ (°)	90.64	88.45	–	92.89
BW at $\Delta A = 1$ dB (MHz)	110	250	–	300
BW at $\Delta\phi = 90 \pm 5$ (MHz)	100	160	–	190
Quad-band branch-line coupler				
$\|S_{11}\|$ (dB)	−16.30	−22.10	−16.50	−16.20
$\|S_{21}\|$ (dB)	−3.71	−3.50	−3.40	−3.53
$\|S_{31}\|$ (dB)	−3.44	−3.48	−3.70	−3.45
$\|S_{41}\|$ (dB)	−17.70	−19.70	−21.30	−17.80
ΔA (dB)	0.27	0.02	0.3	0.08
$\Delta\phi$ (°)	90.10	89.50	90.10	88.60
BW at $\Delta A = 1$ dB (MHz)	95	140	40	390
BW at $\Delta\phi = 90 \pm 5$ (MHz)	110	210	410	>1000

GHz and $f_3 = 4.2$ GHz, resulting in $f_c = 2.85$ GHz. The theoretical design parameters are summarized in Table I.

For the triple-band branch-line coupler it is possible to estimate the performance limitations. In particular, selecting $f_m = f_2$ and $f_N = f_3$ in (17), it follows for the matching $|S_{11}| = -23.2$ dB, for the balance $|S_{21}|/|S_{31}| = 0.082$ dB and for the isolation $|S_{41}| = -23.3$ dB. The photo of the realized triple-band branch-line coupler is shown in Figure 9b.

C. Quad-Band Branch-Line Coupler

For the quad-band branch-line coupler, the selected operating frequencies are $f_1 = 1.5$ GHz, $f_2 = 2.4$ GHz, $f_3 = 3.5$ GHz, and $f_4 = 4.2$ GHz, resulting in $f_c = 2.85$ GHz, as for the triple-band branch-line coupler. f_1, f_2, and f_4 coincide with the triple-band coupler example, resulting in the same theoretical design parameters. The additional design parameters at f_3 are summarized in Table I. Comparing the $Z_{c,i}$ in Table I for the triple-band and quad-band couplers, the condition $Z_{c,m} = Z_{c,2}$ is derived for the quad-band branch-line coupler, resulting in the same Z_c values as for the triple-band branch-line coupler.

As the values of f_1, $f_m = f_2$ and $f_N = f_4$ for the quad-band branch-line coupler are the same of the triple-band one, the same performance limitations are obtained from (17). The photo of the realized quad-band branch-line coupler is shown in Figure 9c.

Comparing the layouts of the three realized branch-line couplers in Figure 9, it is possible to note that the increased number of operating frequencies, from the dual-band to the quad-band branch-line coupler, is achieved simply adding a further ladder cell (series transmission line and parallel stub) to the network based on the Impedance Buffer Methodology.

IV. EXPERIMENTAL RESULTS

Figure 10 reports the simulated and measured scattering parameters of the designed branch-line couplers. In particular, the figure compares simulations based on ideal elements, from hereafter denoted ideal performance, with electromagnetic simulations of the structures.

The ideal performance of the dual-band branch-line coupler (Fig. 10a) confirms the capability of the topology to behave as a perfect branch-line coupler at two frequencies simultaneously. The matching, balance and isolation performance are, in fact, fully satisfied. Passing from ideal to real elements, the performance of the branch-line coupler are degraded, due to the nonideal behavior of actual microstrip lines and cross/tee junctions. Obviously, such an effect is more significant at the highest frequency. However, the measured behaviors are well predicted by the theory and simulations.

The ideal performance of the triple-band branch-line coupler (Fig. 10b) verify the matching, balance and isolation limitations theoretically predicted. Also for this circuit, the greatest degradation has been registered at the highest band, 4.2 GHz, passing to actual elements. However, the measured results show satisfactory levels of

matching, balance and isolation at each of the operating band.

The ideal performance of the quad-band branch-line coupler (Fig. 10c) further verifies the theoretical analysis. For example, the ideal $|S_{11}|$ level of the quad-band branch-line coupler at 1.5 GHz, 2.4 and 4.2 GHz is the same obtained from the triple-band branch-line coupler, while the level at 3.5 GHz is better, as theoretically predicted by analyzing the performance limitations. Finally, the measured performance is well in agreement with the theoretical and simulated one.

Table II summarizes the measured performance for each realized branch-line coupler, reporting also the amplitude ($\Delta A = |S_{21}/S_{31}|$) and phase ($\Delta\phi = \angle S_{21} - \angle S_{31}$) balance at the center frequencies. The bandwidths (BW) at $\Delta A = 1$ dB and $\Delta\phi = 90 \pm 5$ are also added in the table for completeness. Finally, it has to remark that the data reported in Table II exactly refer to the selected operating frequencies, neglecting the little frequency shift the realized prototypes have shown after due to the process variances. In particular, a bit higher frequency shift has been registered for the three-band branch-line coupler prototype.

V. CONCLUSIONS

A novel design approach for multiband branch-line couplers is introduced. The main advantages of this approach are the arbitrary choice of the operating bands, the simple structure, and the ease of fabrication. The complete theoretical analysis of the topology is presented, leading to a closed form equations system for its design. Three couplers based on the proposed structure are implemented for dual-, triple-, and quad-band operation to validate the methodology. Measurement results, in terms of matching, isolation and amplitude and phase balance, show good agreement with simulated ones and demonstrate the desired behavior of the branch-line couplers.

REFERENCES

1. G. Hueber and R.B. Staszewski, Multi-mode/Multi-Band RF Tranceivers for Wireless Communications. Wiley, New Jersey, 2010.
2. J. Lim, C. Park, J. Koo, H. Cha, Y. Jeong, S.-M. Han, and D. Ahn, A balanced power amplifier utilizing the reflected input power, 2009 IEEE International on Symposium on Radio-Frequency Integration Technology, Singapore 2009, pp. 88–91.
3. P. Saad, P. Colantonio, L. Piazzon, F. Giannini, K. Andersson, and C. Fager, Design of a concurrent dual-band 1.8/2.4-ghz gan-hemt doherty power amplifier, IEEE Trans Microwave Theory Tech 60, no. 6 (2012), 1840–1849.
4. P. Colantonio, F. Feudo, F. Giannini, R. Giofre, and L. Piazzon, Design of a dual-band gan doherty amplifier, Conference on Microwave Radar and Wireless Communications, 2010 International, Vilnius (Lithuania) 2010, pp. 1–4.
5. F.R. Shahroury and C.-Y. Wu, The design of low lo-power 60-ghz cmos quadrature-balanced self-switching current-mode mixer, IEEE Microwave Wireless Compon Lett 18 (2008), 692–694.
6. D'Orazio, N.C. Liuzzi, and F.L. Di Alessio, A high performance c-band subharmonic modulator exploiting branch-line couplers as input/output ports, J Electromagn Waves Appl 20 (2006), 489–503.
7. Heidari, M. Heyrani, and M. Nakhkash, A dual-band circularly polarized stub loaded microstrip patch antenna for gps applications, Prog Electromagn Res 92 (2009), 195–208.
8. K. Rawat, M. Rawat, M.S. Hashmi, and F.M. Ghannouchi, Dual-band branch-line hybrid with distinct power division ratio over the two bands, Int J RF Microwave Computer-Aided Eng 23 (2013), 90–98.
9. K.-K. Cheng and F.-L. Wong, A novel approach to the design and implementation of dual-band compact planar 90 deg; branch-line coupler, IEEE Trans Microwave Theory Tech 52 (2004), 2458–2463.
10. H. Zhang and K.J. Chen, A stub tapped branch-line coupler for dual-band operations, IEEE Microw. Wireless Compon Lett 17 (2007), 106–108.
11. C.-L. Hsu, J.-T. Kuo, and C.-W. Chang, Miniaturized dual-band hybrid couplers with arbitrary power division ratios, IEEE Trans Microwave Theory Tech 57 (2009), 149–156.
12. M.-J. Park, Dual-band, unequal length branch-line coupler with center-tapped stubs, IEEE Microwave Wireless Compon Lett 19 (2009), 617–619.
13. K. Rawat, F.M. Ghannouchi, M. Rawat, and M.S. Hashmi, Analysis of frequency-selective impedance loading of transmission lines for dual-band couplers, Int J RF Microwave Computer-Aided Eng 21 (2011), 325–335.
14. M.-J. Park and B. Lee, Dual-band, cross coupled branch line coupler, IEEE Microwave Wireless Compon Lett 15 (2005), 655–657.
15. Z. Atlasbaf and K. Forooraghi, A new dual band branch-line coupler using coupled lines," ISAPE '06. 7th International Symposium on Antennas, Propagation EM Theory, 2006, pp. 1–4.
16. Collado, A. Grau, and F. De Flaviis, Dual-band planar quadrature hybrid with enhanced bandwidth response, IEEE Trans Microw Theory Tech 54 (2006), 180–188.
17. S.Y. Zheng, S.H. Yeung, W.S. Chan, K.F. Man, S.H. Leung, and Q. Xue, Dual-band rectangular patch hybrid coupler, IEEE Trans Microwave Theory Tech 56 (2008), 1721–1728.
18. H. Kim, B. Lee, and M.-J. Park, Dual-band branch-line coupler with port extensions, IEEE Trans Microwave Theory Tech 58 (2010), 651–655.
19. I.-H. Lin, M. DeVincentis, C. Caloz, and T. Itoh, Arbitrary dual-band components using composite right/left-handed transmission lines, IEEE Trans Microwave Theory Tech 52 (2004), 1142–1149.
20. H.-C. Lu, Y.-L. Kuo, P.-S. Huang, and Y.-L. Chang, Dual-band crlh branch-line coupler in ltcc by lump elements with parasite control, IEEE MTT-S International Microwave Symposium Digest (MTT), Anaheim (California) 2010, p. 1.
21. J. Park and Y. Lee, A tunable dual-band branch line coupler based on composite right/left-handed transmission lines, WILEY Microwave Opt Tech Lett 52 (2010), 1955–1958.
22. S. Tanigawa, K. Hayashi, T. Fujii, T. Kawai, and I. Ohta, Tri-band/broadband matching techniques for 3-db branch-line couplers, Microwave Conference, 2007. European, Munich (Germany) 2007, pp. 560–563.
23. C.-Y. Liou, M.-S. Wu, J.-C. Yeh, Y.-Z. Chueh, and S.-G. Mao, A novel triple-band microstrip branch-line coupler with arbitrary operating frequencies, IEEE Microw Wireless Compon Lett 19 (2009), 683–685.
24. F. Lin, Q.-X. Chu, and Z. Lin, A novel tri-band branch-line coupler with three controllable operating frequencies, IEEE Microw Wireless Compon Lett 20 (2010), 666–668.

25. C.-W. Tang and M.-G. Chen, Design of multipassband microstrip branch-line couplers with open stubs, IEEE Trans Microwave Theory Tech 57 (2009), 196–204.
26. M. Durïn-Sindreu, G. Sisï, J. Bonache, and F. Martïn, Planar multi-band microwave components based on the generalized composite right/left handed transmission line concept, IEEE Trans Microw Theory Tech 58 (2010), 3882–3891.
27. L. Piazzon, P. Saad, P. Colantonio, F. Giannini, K. Andersson, and C. Fager, Branch-line coupler design operating in four arbitrary frequencies, IEEE Microwave Wireless Compon Lett 22 (2012), 67–69.
28. M. Pozar, Microwave Engineering. 1em plus 0.5em minus 0.4em, Wiley, New York, 2005.
29. R. Giofrè, P. Colantonio, F. Giannini, and L. Piazzon, A new design strategy for multi frequencies passive matching networks, Microwave Conference, 2007. European, Munich (Germany) 2007, pp. 838–841.
30. N. Nallam and S. Chatterjee, Design of concurrent multiband matching networks, 2011 IEEE International Symposium on Circuits and Systems (ISCAS), Rio de Janeiro (Brazil) 2011, pp. 201–204.
31. Y. Abe, R. Ishikawa, and K. Honjo, Inverse class-f algan/gan hemt microwave amplifier based on lumped element circuit synthesis method, IEEE Trans Microwave Theory Tech 56 (2008), 2748–2753.
32. P. Colantonio, F. Giannini, R. Giofre, and L. Piazzon, A design technique for concurrent dual-band harmonic tuned power amplifier, IEEE Trans Microwave Theory Tech 56 (2008), 2545–2555.
33. F. Corridi, Saggio d'un trattato generale di trigonometria (pag. 128). Pisa: N. Capurro e Comp, 1834.
34. H. Fooks and R.A. Zakarevicius, Microwave engineering using microstrip circuits. Prentice Hall, New York, 1990.

APPENDIX A: DERIVATION OF THE MINIMUM $|S_{11}|$

The aim of this appendix is to demonstrate that the magnitude of (13b) is lower than (13a) and (13c). To fulfill this result, one has to consider that each sine function in (13) has to produce a positive value to obtain positive, that is, realistic, value for the $Z_{c,i}$ from (4). This condition imposes the limitation

$$f_3 < f_1 + f_2 \tag{A1}$$

due to the term

$$\sin\left(\pi \frac{f_3}{f_1 + f_2}\right)$$

in (13a). Obviously, the limitation in (A1) has to be accounted for only if the possible solution in (12a) is adopted for the design.

To demonstrate that the magnitude of (13b) is lower than the one of (13a), one has to verify, regardless of the operating frequencies, the following inequality:

$$\left|\frac{\sin\alpha - \sin\beta}{\sin\alpha + \sin\beta}\right| > \left|\frac{\sin\gamma - \sin\delta}{\sin\gamma + \sin\delta}\right| \tag{A2}$$

where

$$\alpha = \pi \frac{f_1}{f_1 + f_2} \tag{A3}$$

$$\beta = \pi \frac{f_3}{f_1 + f_2} \tag{A4}$$

$$\gamma = \pi \frac{f_1}{f_1 + f_3} \tag{A5}$$

$$\delta = \pi \frac{f_2}{f_1 + f_3} \tag{A6}$$

Accounting for (A3–A6) and (A1), it is possible to note that

$$\sin\alpha > \sin\beta \tag{A7}$$

$$\sin\delta > \sin\gamma \tag{A8}$$

regardless of the operating frequencies, if the definition of f_c in (12) is accounted for. As a consequence, the magnitude in (A2) can be removed, leading to

$$\frac{\sin\alpha - \sin\beta}{\sin\alpha + \sin\beta} > \frac{\sin\delta - \sin\gamma}{\sin\delta + \sin\gamma} \tag{A9}$$

that is equivalent to [33]

$$\frac{\tan\left(\frac{\alpha-\beta}{2}\right)}{\tan\left(\frac{\alpha+\beta}{2}\right)} > \frac{\tan\left(\frac{\delta-\gamma}{2}\right)}{\tan\left(\frac{\delta-\gamma}{2}\right)} \tag{A10}$$

Accounting for (A3–A6) and (A1), the following constraints can be obtained:

$$0 > \frac{\alpha-\beta}{2} > -\frac{\pi}{2} \tag{A11}$$

$$\frac{\pi}{2} < \frac{\alpha+\beta}{2} < \pi \tag{A12}$$

$$0 < \frac{\delta-\gamma}{2} < \frac{\pi}{2} \tag{A13}$$

$$0 < \frac{\delta+\gamma}{2} < \frac{\pi}{2} \tag{A14}$$

The inequality in (A10) is definitely ascertained whether both the followings condition are simultaneously verified:

$$\left|\tan\left(\frac{\alpha-\beta}{2}\right)\right| > \left|\tan\left(\frac{\delta-\gamma}{2}\right)\right| \tag{A15}$$

$$\left|\tan\left(\frac{\alpha+\beta}{2}\right)\right| < \left|\tan\left(\frac{\delta+\gamma}{2}\right)\right| \tag{A16}$$

that, accounting for (A11–A14), can be verified by the following inequalities:

$$\left|\left(\frac{\alpha-\beta}{2}\right)\right| > \left|\left(\frac{\delta-\gamma}{2}\right)\right| \tag{A17}$$

$$\left|\pi - \left(\frac{\alpha+\beta}{2}\right)\right| < \left|\left(\frac{\delta+\gamma}{2}\right)\right| \tag{A18}$$

By substituting (A3–A6) in (A17 and A19), the following conditions are obtained:

$$f_3 > f_2 \tag{A19}$$

$$(f_3 - f_2)^2 > 0 \tag{A20}$$

As the two conditions in (A19 and A20) are always true, the inequality in (19) is verified. The same analysis can be adopted to compare (13b) and (13c). The result confirms that the magnitude of (13b) is lower than the one of (13a) and (13c) regardless of the operating frequencies.

APPENDIX B: SCATTERING PARAMETERS DERIVATION

In Section II, it has been demonstrated that the ABCD-matrix of the multiband quarter-wave transmission line is equal for f_1 and f_3 or f_N in the general case. The multiband branch-line coupler is a combination of multiband quarter-wave transmission lines, consequently its behavior at f_1 is the same as the one at f_N. Hence, the behavior at f_N can be omitted, considering only the one at f_1. At f_1 each branch of the branch-line coupler behaves as a quarter-wave transmission line, whose characteristic impedance is

$$Z_{a,f_1} = Z_{c,a} \cdot \sin\theta_1 \tag{A21}$$

for the horizontal branches in Figure 7b and

$$Z_{b,f_1} = Z_{c,b} \cdot \sin\theta_1 \tag{A22}$$

for the vertical branches in Figure 7b, where $\theta_1 = \frac{\pi}{2}\frac{f_1}{f_c}$. Assuming the definition of $Z_{c,a}$ and $Z_{c,b}$ in (14b) it follows

$$Z_{a,f_1} = Z_a \cdot \sqrt{\frac{\sin\theta_1}{\sin\theta_m}} = \frac{Z_0}{\sqrt{2}} \cdot \sqrt{\frac{\sin\theta_1}{\sin\theta_m}} \tag{A23}$$

$$Z_{b,f_1} = Z_b \cdot \sqrt{\frac{\sin\theta_1}{\sin\theta_m}} = Z_0 \cdot \sqrt{\frac{\sin\theta_1}{\sin\theta_m}} \tag{A24}$$

where $\theta_m = \frac{\pi}{2}\frac{f_m}{f_c}$. The S-parameters of a branch-line coupler as function of the even/odd-mode S-parameters are [34]

$$\begin{aligned} S_{11} &= \frac{S_{11}^{e} + S_{11}^{o}}{2} \quad S_{21} = \frac{S_{21}^{e} + S_{21}^{o}}{2} \\ S_{31} &= \frac{S_{21}^{e} - S_{21}^{o}}{2} \quad S_{41} = \frac{S_{11}^{e} - S_{11}^{o}}{2} \end{aligned} \tag{A25}$$

where the even/odd-mode S-parameters are given by [34]

$$S_{11}^{e} = \frac{Y_0^2 - Y_A^2 + Y_B^2}{Y_0^2 + Y_A^2 - Y_B^2 + j2Y_BY_0} \tag{A26}$$

$$S_{11}^{o} = \frac{Y_0^2 - Y_A^2 + Y_B^2}{Y_0^2 + Y_A^2 - Y_B^2 - j2Y_BY_0} \tag{A27}$$

$$S_{21}^{e} = -j2\frac{Y_AY_0}{Y_0^2 + Y_A^2 - Y_B^2 + j2Y_BY_0} \tag{A28}$$

$$S_{21}^{o} = -j2\frac{Y_AY_0}{Y_0^2 + Y_A^2 - Y_B^2 - j2Y_BY_0} \tag{A29}$$

where $Y_0 = 1/Z_0$ is the port admittance, Y_A and Y_B are the characteristic admittance of the series quarter-wave transmission line and the admittance of the $\lambda/8$ open stub due to the even/odd-mode analysis, respectively. Applying (A23 and A24) at f_1 yields

$$Y_A = \frac{\sqrt{2}}{Z_0} \cdot \sqrt{\frac{\sin\theta_m}{\sin\theta_1}} \tag{A30}$$

$$Y_B = \frac{1}{Z_0} \cdot \sqrt{\frac{\sin\theta_m}{\sin\theta_1}} \tag{A31}$$

Replacing (A30 and A31) in (A26–A29) and, subsequently, in (A25), the S-parameters of the multi-band branch-line coupler at f_1 are inferred:

$$S_{11,f_1} = \frac{\sin^2\theta_1 - \sin^2\theta_m}{\sin^2\theta_1 + 6\sin\theta_1\sin\theta_m + \sin^2\theta_m} \tag{A32}$$

$$S_{21,f_1} = -j2\sqrt{2}\frac{\sqrt{\sin\theta_1\sin\theta_m}(\sin\theta_1 + \sin\theta_m)}{\sin^2\theta_1 + 6\sin\theta_1\sin\theta_m + \sin^2\theta_m} \tag{A33}$$

$$S_{31,f_1} = -4\sqrt{2}\frac{\sin\theta_1\sin\theta_m}{\sin^2\theta_1 + 6\sin\theta_1\sin\theta_m + \sin^2\theta_m} \tag{A34}$$

$$S_{41,f_1} = -j2\frac{\sqrt{\sin\theta_1\sin\theta_m}(\sin\theta_1 - \sin\theta_m)}{\sin^2\theta_1 + 6\sin\theta_1\sin\theta_m + \sin^2\theta_m} \tag{A35}$$

Following the same procedure for f_m, it is possible to derive:

$$Z_{a,f_m} = Z_a \cdot \sqrt{\frac{\sin\theta_m}{\sin\theta_1}} = \frac{Z_0}{\sqrt{2}} \cdot \sqrt{\frac{\sin\theta_m}{\sin\theta_1}} \tag{A36}$$

$$Z_{b,f_m} = Z_b \cdot \sqrt{\frac{\sin\theta_m}{\sin\theta_1}} = Z_0 \cdot \sqrt{\frac{\sin\theta_m}{\sin\theta_1}} \tag{A37}$$

therefore

$$Y_A = \frac{\sqrt{2}}{Z_0} \cdot \sqrt{\frac{\sin\theta_1}{\sin\theta_m}} \tag{A38}$$

$$Y_B = \frac{1}{Z_0} \cdot \sqrt{\frac{\sin\theta_1}{\sin\theta_m}} \tag{A39}$$

and finally

$$S_{11,f_m} = \frac{\sin^2\theta_m - \sin^2\theta_1}{\sin^2\theta_1 + 6\sin\theta_1\sin\theta_m + \sin^2\theta_m} \tag{A40}$$

$$S_{21,f_m} = -j2\sqrt{2}\frac{\sqrt{\sin\theta_1\sin\theta_m}(\sin\theta_1 + \sin\theta_m)}{\sin^2\theta_1 + 6\sin\theta_1\sin\theta_m + \sin^2\theta_m} \tag{A41}$$

$$S_{31,f_m} = -4\sqrt{2}\frac{\sin\theta_1\sin\theta_m}{\sin^2\theta_1 + 6\sin\theta_1\sin\theta_m + \sin^2\theta_m} \tag{A42}$$

$$S_{41,f_m} = -j2\frac{\sqrt{\sin\theta_1\sin\theta_m}(\sin\theta_m - \sin\theta_1)}{\sin^2\theta_1 + 6\sin\theta_1\sin\theta_m + \sin^2\theta_m} \tag{A43}$$

Comparing (A32–A35) and (A40–A43), one can easily show that these expressions lead to identical matching, balance and isolation properties at f_1 and f_m. Moreover, (A33–A34) and (A41–A42) demonstrate that the adopted topology satisfies the quadrature condition for both f_1 and f_m, that is, 90 of phase shift between S_{21} and S_{31}.

BIOGRAPHIES

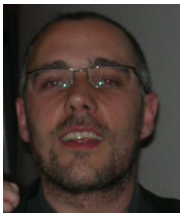

Luca Piazzon received the B.S. degree and the M.S. degree in Electronic Engineering from the University of Roma ''Tor Vergata'', Italy, in 2004 and 2007, respectively. In 2011 he obtained the Ph.D. degree in Systems and Technologies for Space Applications from the same University, where he become a Researcher in 2013. His main research activities concern the fields of nonlinear and linear microwave circuit design methodologies, linear and nonlinear characterization and modelling techniques.

Paul Saad received the B.S. degree in electrical engineering from the Lebanese University, Beirut, Lebanon, in 2005, the M.S. degree in RF and Microwave engineering from university of Gävle, Sweden, in 2007, and the Ph.D. degree from Chalmers University of Technology, Sweden, in 2012.

His research concerns the design of high-efficiency multi-band and wide-band power amplifiers.

Mr. Saad was the recipient of the 2009 Certificate of High Achievement and the 2010 First Place Award of the Student High Efficiency Power Amplifier Design Competition of the IEEE Microwave Theory and Techniques Society (IEEE MTT-S) International Microwave Symposium (IMS).

Paolo Colantonio was born in Roma, Italy on March 22, 1969. He received the Electronic Engineering degree and Ph.D. degree in Microelectronics and Telecommunications from the University of Roma ''Tor Vergata'', Italy, in 1994 and 2000, respectively.

In 1999 he became a Research Assistant with the University of Roma ''Tor Vergata'', where, since 2002, he has been a Professor of Microwave Electronics. He authored or co-authored more than one hundred and fifty scientific papers. He authored the book *High Efficiency RF and Microwave Solid State Power Amplifiers* (Wiley, 2009). His main research activities are in the field of nonlinear microwave circuit design methodologies, nonlinear analysis techniques and modelling of microwave active devices.

Franco Giannini was born in Galatina (LE) Italy, on November 9, 1944. He received the Electronics Engineering (summa cum laude) from the University of Roma ''La Sapienza,'' Rome, Italy, in 1968. Since 1980, he has been a Full Professor of applied electronics with the University of Rome Tor Vergata, Rome, Italy. Since 2001, he has been an Honorary Professor with the Warsaw University of Technology (WUT), Warsaw, Poland. He has been involved with problems concerning modelling, characterization, and design methodologies of linear and nonlinear active microwave components, circuits, and subsystems, including monolithic microwave integrated circuits (MMICs). He is a consultant for various national and international industrial and governmental organizations, including the International Telecommunication Union and the European Union. He has authored or co-authored over 430 scientific papers. Prof. Giannini is a member of the Board of Directors of the Italian Space Agency (ASI). He is president of the GAAS Association. He has also been a member of numerous committees of international scientific conferences. He was the recipient of the Doctor Honoris Causa degree from the WUT in 2008.

Kristoffer Andersson received the M.Sc. degree and Ph.D. in Electrical Engineering from Chalmers University of Technology, Goteborg, Sweden, in 2001 and 2006 respectively. His research interests are in the area of characterization and modeling of wide bandgap transistors.

Christian Fager received the M.Sc. and Ph.D. degrees in Electrical Engineering and Microwave Electronics, from Chalmers University of Technology, Sweden, in 1998 and 2003, respectively. He is currently an Associate Professor and project leader in the GigaHertz Centre at the Microwave Electronics Laboratory. In 2002 he received the Best Student Paper Award at the IEEE International Microwave Symposium. His research interests are in the areas of large signal transistor modeling and high efficiency power amplifier architectures.